Synthetic Aperture Radar Applications in Coastal Waters

Martin Gade[1]

[1] ***Institut für Meereskunde, Universität Hamburg, 20146 Hamburg, Germany,***
Tel: +49 40 42838-5450, Fax: +49 40 42838-7471,
Email: Martin.Gade@uni-hamburg.de

Abstract

A Synthetic Aperture Radar (SAR) is an active microwave sensor, which provides radar images at high spatial resolution. SARs have been flying on several earth-orbiting satellites since the late 1970s, thereby providing a great deal of high-resolution radar imagery of coastal regions. We provide an overview of several oceanic and atmospheric processes and phenomena in the marine coastal environment that can be seen on SAR imagery. Among them are wind and wave fields, oceanic internal waves, marine surface films and oil pollution, sea bottom topography, ships (vessels), and heavy rain. We illustrate the wealth of information that can be inferred from radar imagery with spatial resolutions reaching a few decimeters and demonstrate the benefit of SAR data to scientists, coastal managers, agencies, and public or commercial bodies.

Introduction

Active microwave sensors such as radar transmit electromagnetic waves (usually in pulses) with wavelengths in the decimeter to millimetre range, and they record the radiation that is scattered back from a target. If the target is wet, or moist, then the penetration depth of the microwaves is rather small, and in case of salinity it is only a fraction of the microwave's wavelength. Therefore, microwaves "feel" only the ocean's surface, and the strength of the backscattering mainly depends on the surface roughness (in case of an ideally flat surface the transmitted microwaves would simply be scattered away from the antenna). This is, very briefly, the main background of the use of radar sensors for the detection of ocean surface properties in coastal regions.

The spatial resolution of an imaging radar basically depends on the antenna size: larger antennas allow imaging at finer resolution, and vice versa. This fact, however, would make it impossible to use a radar aboard a satellite, since the antenna length (i.e., its aperture) would have to be on the order of a kilometre, in order to allow for "proper" spatial resolutions of several meters at most. This is why the radar's real aperture is synthetically enhanced by taking advantage of the phase, or Doppler, shift of the backscattered signal (with respect to the transmitted signal). This technique, along with further sophisticated additions, allows some modern synthetic aperture radar (SAR) systems to provide radar images with pixel sizes reaching below 1 m², even though the data were acquired at orbit heights of several 100 kilometers. Table 1 provides a historical overview of the main (civilian) spaceborne SAR systems as of today.

SAR sensors operate at GHz frequencies, in certain spectral ranges (bands) of the electromagnetic spectrum: L-band means frequencies slightly above 1 GHz (wavelengths slightly below 30 cm), S-band frequencies are between 2.5 GHz and

Table 1: History of spaceborne SAR sensors.

Year	Satellite	Band	Inc.Angle	Polarization
1978	SEASAT (USA)	L (1.3 GHz)	23°	HH
1981	SIR-A (USA)	L (1.3 GHz)	50°	HH
1984	SIR-B (USA)	L (1.3 GHz)	15°-65°	HH
1991	ERS-1 (Europe)	C (5.3 GHz)	23°	VV
1991	ALMAZ-1 (USSR)	S (3.0 GHz)	30°-60°	HH
1992	JERS-1 (Japan)	L (1.3 GHz)	39°	HH
1994	SIR-C/X-SAR (USA, Germany)	L (1.3 GHz), C (5.3 GHz), X (9.6 GHz)	15°-55°	HH, HV, VV, VH (SIR-C), VV (X-SAR)
1995	ERS-2 (Europe)	C (5.3 GHz)	23°	VV
1995	Radarsat-1 (Canada)	C (5.3 GHz)	20°-50°	HH
2000	SRTM (USA, Germany)	C (5.3 GHz), X (9.6 GHz)	54°	HH, VV (C), VV (X)
2002	ENVISAT (Europe)	C (5.3 GHz)	15°-45°	HH, HV, VV, VH
2006	ALOS-1 (Japan)	L (1.3 GHz)	8°-60°	HH, HV, VV, VH
2007	TerraSAR-X (Germany)	X (9.7 GHz)	15°-60°	HH, HV, VV, VH
2007	Radarsat-2 (Canada)	C (5.3 GHz)	10°-60°	HH, HV, VV, VH
200710	COSMO-SkyMed 1-4 (Italy)	X (9.6 GHz)	20°-59°	HH, HV, VV, VH
2010	TanDEM-X (Germany)	X (9.7 GHz)	15°-60°	HH, HV, VV, VH
2014	ALOS-2 (Japan)	L (1.3 GHz)	8°-70°	HH, HV, VV, VH
2014	Sentinel-1A (Europe)	C (5.4 GHz)	20°-45°	HH/HV, VV/VH

3 GHz (12 cm to 10 cm), C-band above 5 GHz (6 cm), and X-band around 10 GHz (3 cm). The radar wavelength is important, since the size of the surface roughness (in the case of the ocean the length of the surface waves) responsible for the backscattering

is on the same order (Wright, 1968). Typical incidence angles (i.e. the angle between nadir and the radar look direction) are ranging from 15° to 60°, and the two letters specifying the radar polarization refer to the polarization of the transmitted and of the received microwaves (H = horizontal, V = vertical). For a comprehensive scientific background and a detailed description of various SAR applications in the marine environment the reader is referred to Jackson and Apel (2004).

SAR Image Examples

A first example of a SAR image is shown in Fig. 1: the image of the Romanian Black Sea coast, between the cities of Constanța (in the north) and Mangalia (in the south), was acquired by the German TerraSAR-X on November 6, 2008, at 04:17 UTC (image dimensions are 19 km × 35 km, mean incidence angle is 37.3°, pixel size is approx. 1.5 m × 1.5 m). Throughout the image, parallel streaks reaching from the coast far offshore (A) are manifestations of a north-westerly wind blowing at the time of image acquisition. Wind roughens the sea surface, and the backscattered radar power therefore depends on the wind speed (Stoffelen and Anderson, 1997). The streaky nature of the wind field is caused not only by the orography or obstacles on the coast, but also (particularly further offshore) by atmospheric boundary rolls, i.e., turbulent elongated rolls in the lower atmosphere (Foster, 2013).

Several ships off the port of Constanța are visible as bright spots (B), since metal is a perfect reflector of microwaves. In addition, one larger ship just entered the imaged area from the east (right image center). Its wake can clearly be seen, but the ship appears to be shifted northward from the wake; this so-called ship-off-the-wake effect is a well-known artefact of SAR images and is due to the synthetic enhancement of the radar's aperture mentioned above and depends on the target's speed and moving direction (Graf and Guthart, 1969).

Several dark patches (C) can be found in the image, which apparently are not wind-induced. Those patches are due to mineral oil that was released recently (likely during the night – the image was acquired in the early morning hours, just before sunrise) and that flattens the water surface locally. This image nicely shows why spaceborne SAR sensors are state-of-the-art instruments for the detection of marine oil pollution (Brekke and Solberg, 2005).

Another example, a SAR image of the Bulgarian Black Sea coast, between the city of Varna and Cape Kaliakra, acquired on October 21, 2014, at 15:59 UTC by the C-band SAR aboard the European Sentinel-1A satellite, is shown in Fig. 2 (this is a VV-polarization image, pixel size is 10 m × 10 m, mean incidence angle is 39°). In general,
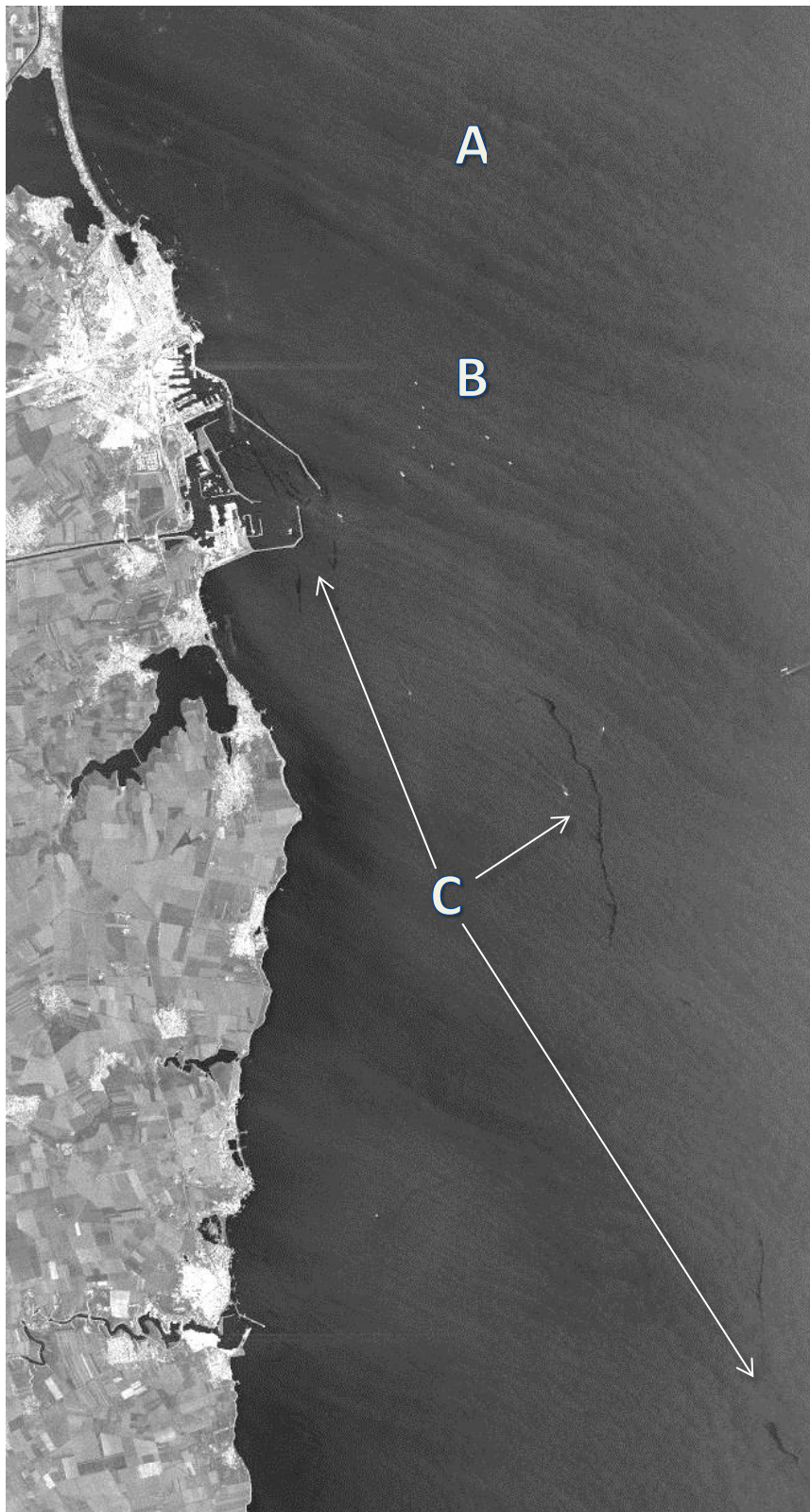
Fig. 1: TerraSAR-X image (19 km × 35 km) of the Bulgarian Black Sea coast, between the cities of Constanţa (north) and Mangalia (south), acquired on November 6, 2008, at 04:17 UTC. Note the signatures of offshore blowing winds (A), of ships (B), and of oil pollution (C). © DLR 2008.

the sea surface is uniformly grey, indicating a uniform roughness (and wind), though in the upper (northern) part wind shadowing and marine surface films result in a smoother sea surface and, therefore, in a reduced radar backscattering (darker areas). In addition,

in the lower left part of the image, the outflow of the Lake Varna can be identified through a dark patch, again, indicating a smooth water surface.

Two regions, each of size 12 km × 9 km, have been selected for a closer look. In the lower left corner of the south-western region, again, ships show up as bright spots. In the region's upper right part many dark parallel filaments can be seen, which are due to natural surface films accumulating along the main (shear) current lines (Gade et al., 2013). Those films dampen the small-scale waves (Alpers and Hühnerfuss, 1989) and, therefore, reduce the radar backscattering. One dark feature, however, is not aligned with the local currents (see the white arrow) and is likely to be due to a mineral oil spill, whose total length is about 6 km. The north-eastern region lies in the area which is
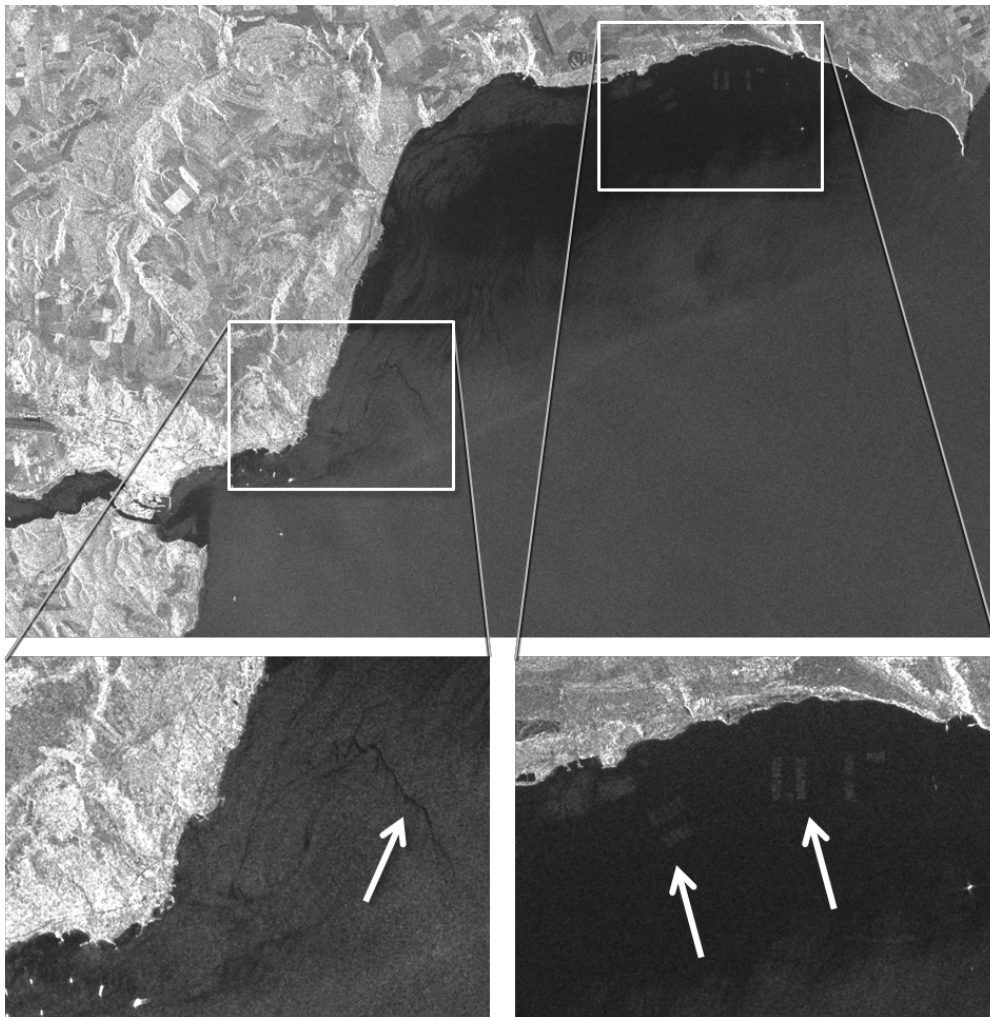

Fig. 2: Sentinel-1A SAR image (55 km × 35 km) of the Bulgarian Black Sea coast between Varna (south-west) and Cape Kaliakra (north-east), acquired on October 21, 2014, at 15:59 UTC. See text for more details. © ESA 2014.

affected by wind shadowing and, therefore, shows up dark on the SAR image. Rectangular structures, however, can be delineated in the region's center and are due to fish farms, whose frames and constructions reflect the microwaves. The fish may be one (biogenic) source of the natural surface films encountered in that area.

Natural surface films accumulate along shear current lines and thereby can be tracers of turbulent ocean surface features such as sub-mesoscale oceanic eddies. Fig. 3 shows an example of several spiral eddies observed in the north-eastern Black Sea (Gade et al., 2013). Although the natural surface films are present on the water surface (and, therefore, visible on SAR imagery) only at low to moderate wind speeds (2 m/s – 7 m/s), the analysis of large numbers of SAR images with respect to imprints of oceanic eddies can provide statistical information on near-coastal turbulent dynamics (Karimova, 2012).
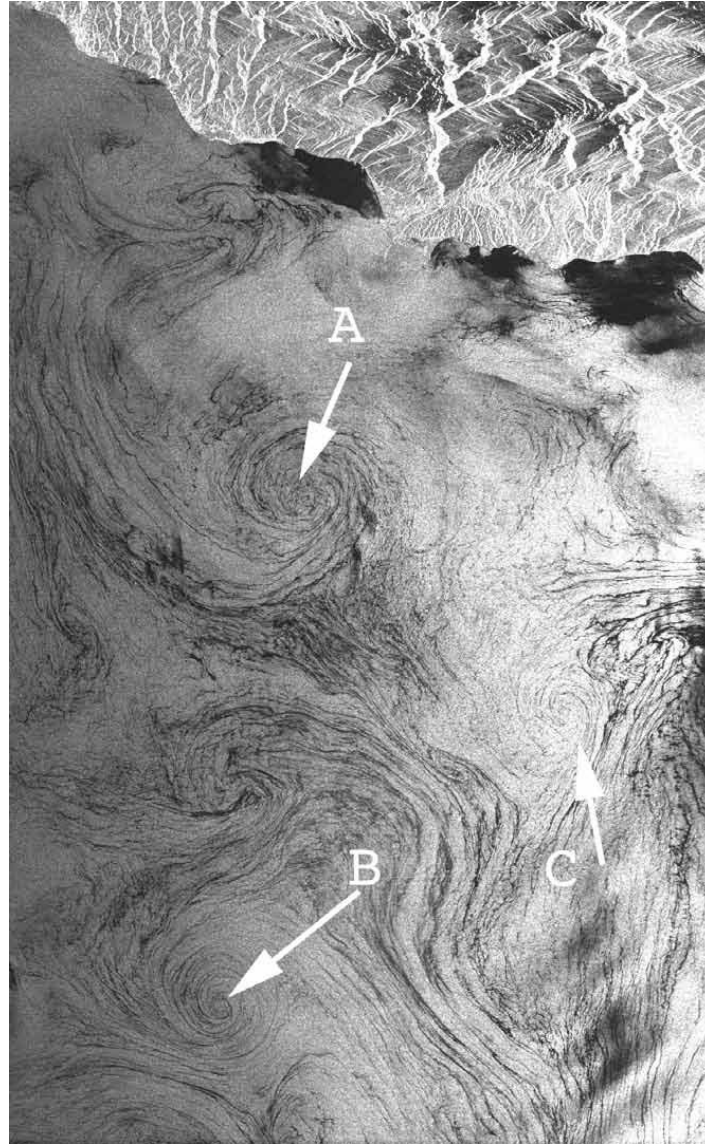

Fig. 3: Envisat ASAR image of the north-eastern Black Sea, acquired on May 10, 2007, at 07:37 UTC. Natural surface films accumulating along shear current lines mark spiral eddies (A, B, C). © ESA 2007. Taken from Gade et al. (2013).

Ocean surface waves are imaged by SAR sensors, and their imprints can be delineated from SAR images such as that shown in Fig. 4. The Radarsat-1 SAR image (C-Band, HH-polarization, 29 km × 28 km) of Point Reyes on the Californian Pacific Coast was acquired on November 22, 2001, at 22:39 UTC and shows signatures of long ocean surface waves approaching the coast from the west. Depending on their length and height (amplitude), however, the SAR imaging of those waves may become strongly non-linear, thereby making it difficult to infer quantitative information on the wave field

from SAR imagery (Alpers and Rufenach, 1979). Clearly visible in Fig. 4 is the refraction of the ocean waves when they are reaching the coast, and when they are propagating around Point Reyes in particular. In certain cases, i.e. without the above-mentioned non-linearities, this effect can be used to infer sea bottom topography in shallow areas from SAR imagery (Brusch et al., 2011).

Fig. 5 shows another example of wind field variations visible on SAR imagery. The image was acquired by the SAR aboard ERS-1 on September 8, 1992, at 21:13 UTC and shows the southern Tyrrhenian Sea and the Strait of Messina between Sicily (lower left) and Calabria (lower right). South of the Strait manifestations of oceanic internal waves can be seen through parallel, concentric bright and dark features (Alpers, 1985). The upper image part is dominated by cloudy signatures (A) originating from atmospheric convection cells: the up- or downdraft within those cells, overlaid to the
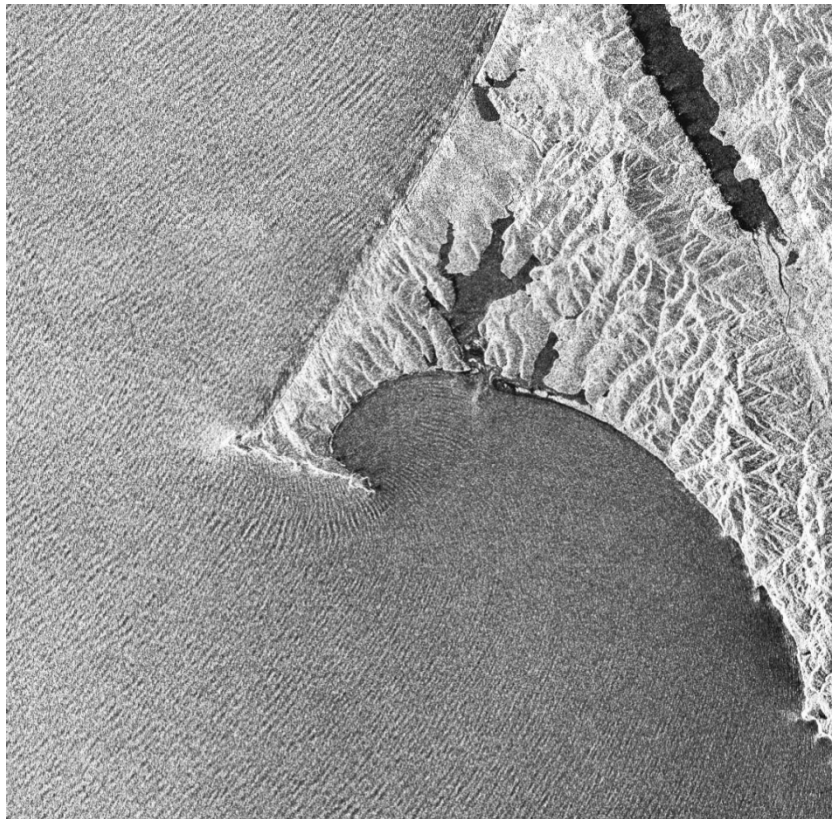

Fig. 4: Radarsat-1 SAR image (29 km × 28 km) of Point Reyes on the Californian Pacific Coast, acquired on November 22, 2001, at 22:39 UTC and showing signatures of long ocean waves. © CSA 2001.

background wind field, causes circular wind-field patterns at the water surface, which in turn result in circular (or cloudy) patterns in the SAR images. In addition, on the north coasts of Sicily and Calabria, offshore blowing wind fields can be delineated through bright "tongues" reaching off the coast (B). Those wind fields are due to katabatic wind circulation in the night hours, when the land is cooling down and the sea is still warm, thereby causing a downdraft over land and an updraft over sea, and therefore an offshore directed wind – whose extent can be inferred from SAR imagery like that shown in Fig. 5.

The roughness of the sea surface may be changed not only by the wind (increasing it) or by marine surface films (decreasing it), but also by currents, either directly or in combination with the local wind field. Fig. 6 shows as an example a TerraSAR-X image of the German North Sea coast, acquired on August 21, 2008, at 05:50 UTC, about 2.5 hours before low tide in that area. Strong offshore ebb flows through the tidal channels cause brighter structures in the lower and middle parts of the image, where the water was flowing against the south-westerly wind and where
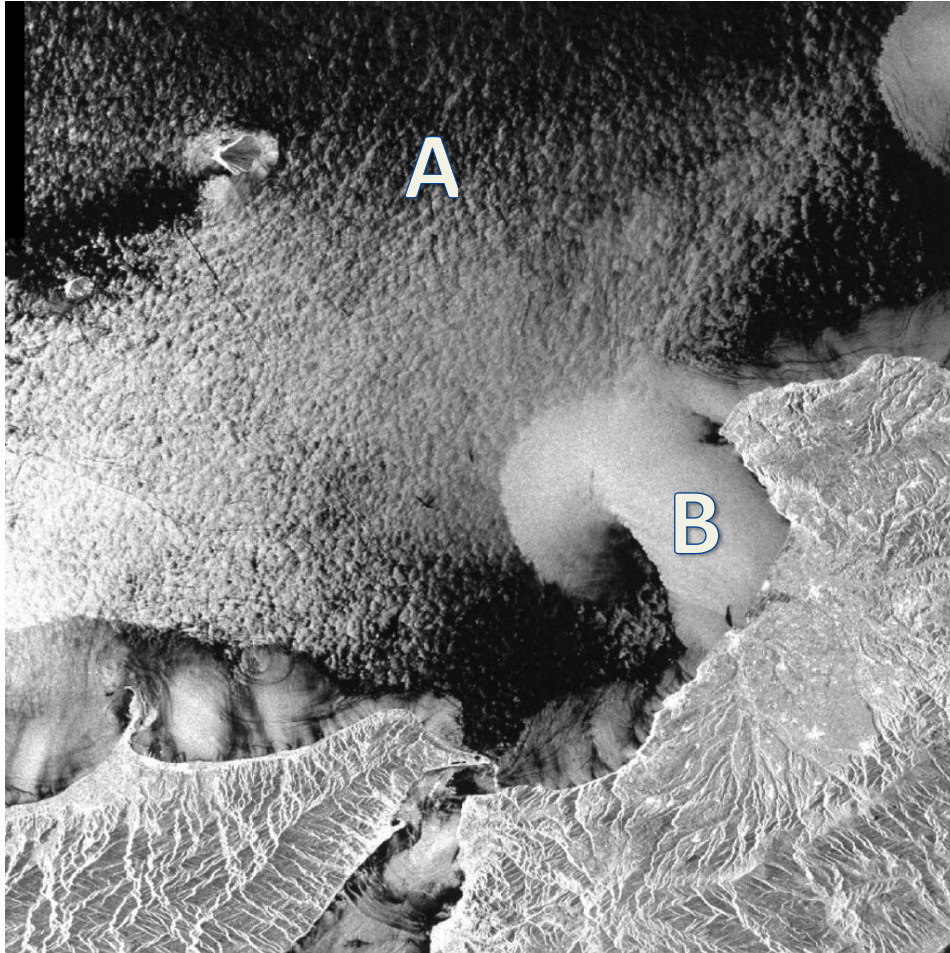

Fig. 5: ERS-1 SAR image (100 km × 100 km) of the Tyrrhenian Sea, north of the Strait of Messina, acquired on September 8, 1992, at 21:13 UTC. Katabatic winds cause the bright area marked with (A), whereas the overall patchy structure in most parts of the image (B) is due to atmospheric convecton cells. (c) ESA 1992.
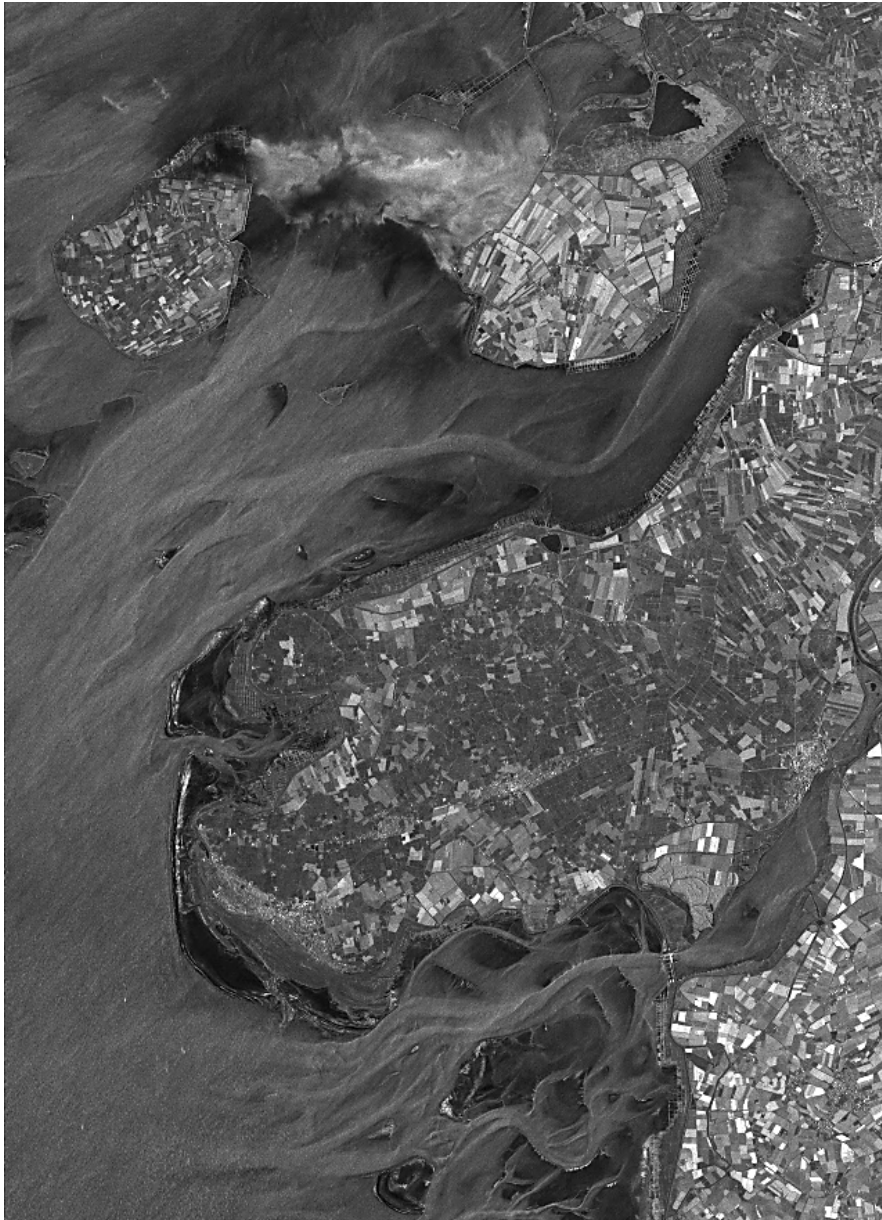
Fig. 6: TerraSAR-X image (30 km × 40 km) of the German North Sea coast, acquired on August 21, 2008, at 05:50 UTC, during ebb tide. The irregular bright patches in the upper part of the image are due to heavy rain. © DLR 2008.

the effective wind speed ("felt" by the water surface) was increased. Images like that shown in Fig. 6 help understanding small-scale coastal hydrodynamics and developing and validating numerical current models.

Another interesting feature can be seen in the upper part of Fig. 6, namely the bright irregular patches between the two islands (Pellworm in the west and Nordstrand in the east – that latter already being connected with the land thanks to land reclamation). These signatures, certainly being caused by a local increase in the surface roughness, are due to heavy rain in that area. The rain drops, impinging on the sea surface, cause additional roughness, which in turn results in a locally increased radar backscatter.

In Fig. 7 a final example is shown demonstrating how current variations can manifest in SAR imagery. The image was acquired by the ERS-1 SAR on July 8, 1995,

at 02:34 UTC and shows the Chinese Yellow Sea coast. Dry-fallen intertidal flats can be seen in the image center; however, the variations of image brightness throughout the SAR image are caused by underwater bottom topography (Alpers and Hennings, 1984), which, in combination with numerical current models can be inferred from SAR images like the one shown herein (or vice versa).

Conclusions

After a short introduction and some background information, we have demonstrated that SAR imagery can be used to infer a number of oceanic and atmospheric parameters in coastal areas. Marine pollution can be monitored, atmospheric dynamics can be quantified more easily, and wave and current fields can be calculated or used to infer underwater bottom topography. However, we also note that most SAR image features can be observed only at certain wind speed ranges:

Fig. 7: ERS-1 SAR image (100 km × 100 km) of the Chinese Yellow Sea coast, north of the Yangtse estuary, acquired on July 8, 1995, at 02:34 UTC. Off the mainland coast signatures of underwater bottom topography and of dry-fallen intertidal flats can be seen as bright and dark features, respectively. (c) ESA 1995.

high winds will always be the dominating cause of the surface roughness, thereby covering the effects that might be of interest. For the sake of shortness, Table 2 provides a list of features that can be seen on SAR imagery, along with their length scales, measurement and imaging parameters, and the wind speed range, at which they are observable (Holt, 2004).

Table 2: Features on SAR imagery, after Holt (2004).

Feature	Scale	Derived Measurement	Imaging Mechanism	Wind [m s⁻¹]
Ocean Features				
Surface Waves	100 – 600 m wavelength	Wavelength Propagation direction Wave height	Tilt Hydrodynamic Velocity Bunching	3 – 40
Internal Waves	0.3 – 3 km wavelength	Wavelength Direction Amplitude Mixed layer depth	Convergence/Divergence Surfactants	2 – 10
Internal Tides	10 – 20 km	Wavelength Direction	Interaction of centimeter Waves/Currents/Surfactants	3 – 7
Currents and Fronts	1 – 100 km	Location Shear Strain Velocity	Shear/Convergence Convergence Wind stress Surfactants	3 – 10 3 – 10 3 – 10 3 – 7
Eddies	1 – 200 km diameter	Location and source Diameter Velocity Shear Strain	Shear/Convergence Wind Stress Surfactants	3 – 10 3 – 10 3 – 7
Shallow Water Bathymetry	5 – 50 m depth	Location/change detection Current velocity Depth	Convergence	3 – 12
Atmospheric Features				
Surface Winds	> 1km grid	Wind speed Wind direction	Wind stress Indirectly via windrows, models, or sensors	3 – 25
Roll Vortices	1 - 5 km wavelength	Boundary Layer: Stratification	Wind stress	3 – 15
Gravity Waves	2 - 10 km wavelength	Height Turbulence spectrum Drag coefficient	Wind stress	3 – 15
Rain Cells	2 - 40 km diameter	Rain rate	Wind stress Rain damping	3 – 15
Marine Surface Films				
Biogenic Surfactants	> 100m² area	Areal extent	Convergence	2 – 8
Mineral Oils	> 100m² area	Areal extent	Seeps Ship discharge Run-off	3 – 15

References

Alpers, W. (1985), "Theory of radar imaging of internal waves", *Nature, 314*, 245-247.

Alpers, W.; Hennings, I. (1984), "A theory of the imaging mechanism of underwater bottom topography by real and synthetic aperture radar". *J Geophys. Res. 89*, 10529-10546.

Alpers, W., and Hühnerfuss, H. (1989), "The damping of ocean waves by surface films: a new look at an old problem", *J. Geophys. Res., 94,* 6251-6265.

Alpers, W., and Rufenach, C.L. (1979), "The effect of orbital motions on synthetic aperture radar imagery of ocean waves", *IEEE Trans. Antennas Propag., 27*, 685-690.

Brekke, C., and A.S. Solberg (2005), "Oil spill detection by satellite remote sensing", *Remote Sens. Environ., 95(1)*, 1-13.

Brusch, S., Held, P., Lehner, S., Rosenthal, W. and Pleskachevsky, A. (2011), "Underwater bottom topography in coastal areas from TerraSAR-X data", *Intern. J. Remote Sens.*, 32, 4527-4543.

Foster, R. (2013), "Signature of Large Aspect Ratio Roll Vortices in Synthetic Aperture Radar Images of Tropical Cyclones", *Oceanography, 26(2)*, 58-67.

Gade, M., Byfield, V., Ermakov, S., Lavrova, O., and Mitnik, L. (2013), "Slicks as Indicators for Marine Processes", *Oceanography, 26(2)*, 138-149.

Graf, K.A., and Guthart, H. (1969), "Velocity effects in synthetic apertures", *IEEE Trans. Antennas Propag., 17*, 541-546.

Holt, B. (2004), "SAR Imaging of the Ocean Surface", In: Jackson, C.R., Apel, J.R. (Eds.) *Synthetic Aperture Radar Marine User's Manual*, NOAA NESDIS Office of Research and Applications, Washington DC, 25-79.

Jackson, C.R., and Apel, J.R. (2004), *"Synthetic Aperture Radar Marine User's Manual"*, NOAA NESDIS Office of Research and Applications, Washington DC, 464 p.

Karimova, S.S. (2012), "Spiral eddies in the Baltic, Black and Caspian seas as seen by satellite radar data", *Adv. Space Res., 50*, 1107-1124.

Stoffelen, A., Anderson, D.L.T. (1993), "Wind retrieval and ERS-1 scatterometer radar backscatter measurements", *Adv. Space Res., 13*, 53-60.

Wright, J.W. (1968), "A new model for sea clutter", *IEEE Trans Antennas Propag., 16*, 217-223.